Article

Self-organized intracellular twisters

Check for updates

Sayantan Dutta [1,2,6], Reza Farhadifar [2,6], Wen Lu [3], Gokberk Kabacaoğlu [2], Robert Blackwell [2], David B. Stein [2], Margot Lakonishok[3], Vladimir I. Gelfand [3], Stanislav Y. Shvartsman[1,2,4] & Michael J. Shelley [2,5] ✉

Life in complex systems, such as cities and organisms, comes to a standstill when global coordination of mass, energy and information flows is disrupted. Global coordination is no less important in single cells, especially in large oocytes and newly formed embryos, which commonly use fast fluid flows for dynamic reorganization of their cytoplasm. These cytoplasmic streaming flows have been proposed to spontaneously arise from hydrodynamic interactions among cortically anchored microtubules loaded with cargo-carrying molecular motors. Here, we combine modelling and simulation with live imaging to investigate such flows in the *Drosophila* oocyte. Using a fast, accurate and scalable numerical approach to investigate fluid–structure interactions of thousands of flexible fibres, we demonstrate the robust emergence and evolution of cell-spanning vortices—or twisters—in three-dimensional cellular geometries. These twister flows, dominated by a near-rigid-body rotation with secondary toroidal components, reproduce the variety of experimental observations. In cells, these flows are probably involved in rapid mixing and transport of ooplasmic components.

Cytoplasmic streaming, first described in 1774 by Bonaventura Corti[1], regulates a wide range of intracellular processes, especially when large cell size makes diffusion and motor-driven transport too slow for efficient intracellular transport and mixing[2–10]. The types of cytoplasmic flows can vary significantly among cells and over different stages of cell development, from random streaming in early fly oocytes to circulation flows observed in plants and later oocytes, to shuttle streaming found in slime moulds[11,12]. Cytoplasmic flows are commonly driven by forces originating from the cell cortex, where motor proteins carry cargo along cytoskeletal filaments and so entrain the fluid[13]. The formation of macroscopic flows in cells requires an alignment in motor movements across many filaments. In some cells, such as the algae *Chara*, this alignment originates from the organization of actin filaments at earlier developmental stages and can be viewed as providing static boundary conditions for the flow problem[6,14]. In others, like oocytes of the fruit fly *Drosophila*, our focus here, motors move on a cytoskeletal bed of flexible microtubules, and their alignment and direction were proposed to arise by means of self-amplifying feedback between motor-induced cytoplasmic flows and collective deformations of the microtubule bed[15]. Understanding how these large-scale flows emerge in a system of hydrodynamically coupled deformable fibres is highly non-trivial because of strong geometric nonlinearities and widely separated spatiotemporal scales. Here, we present a versatile modelling approach for tackling this challenge and show how it can be combined with experiments in the *Drosophila* oocyte to provide general insights into self-organized cytoplasmic streaming.

The cytoplasm of the developing *Drosophila* oocyte remains relatively quiescent for the first three days of oogenesis. During this time, diffusion and directed transport are used to localize several molecular factors needed for the patterning of the future embryo[9,16].

[1]Department of Chemical and Biological Engineering, Princeton University, Princeton, NJ, US. [2]Center for Computational Biology, Flatiron Institute, New York, NY, US. [3]Department of Cell and Developmental Biology, Feinberg School of Medicine, Northwestern University, Chicago, IL, US. [4]Department of Molecular Biology and Lewis Sigler Institute of Integrative Genomics, Princeton University, Princeton, NJ, US. [5]Courant Institute of Mathematical Sciences, New York University, New York, NY, US. [6]These authors contributed equally: Sayantan Dutta, Reza Farhadifar. ✉e-mail: mshelley@flatironinstitute.org
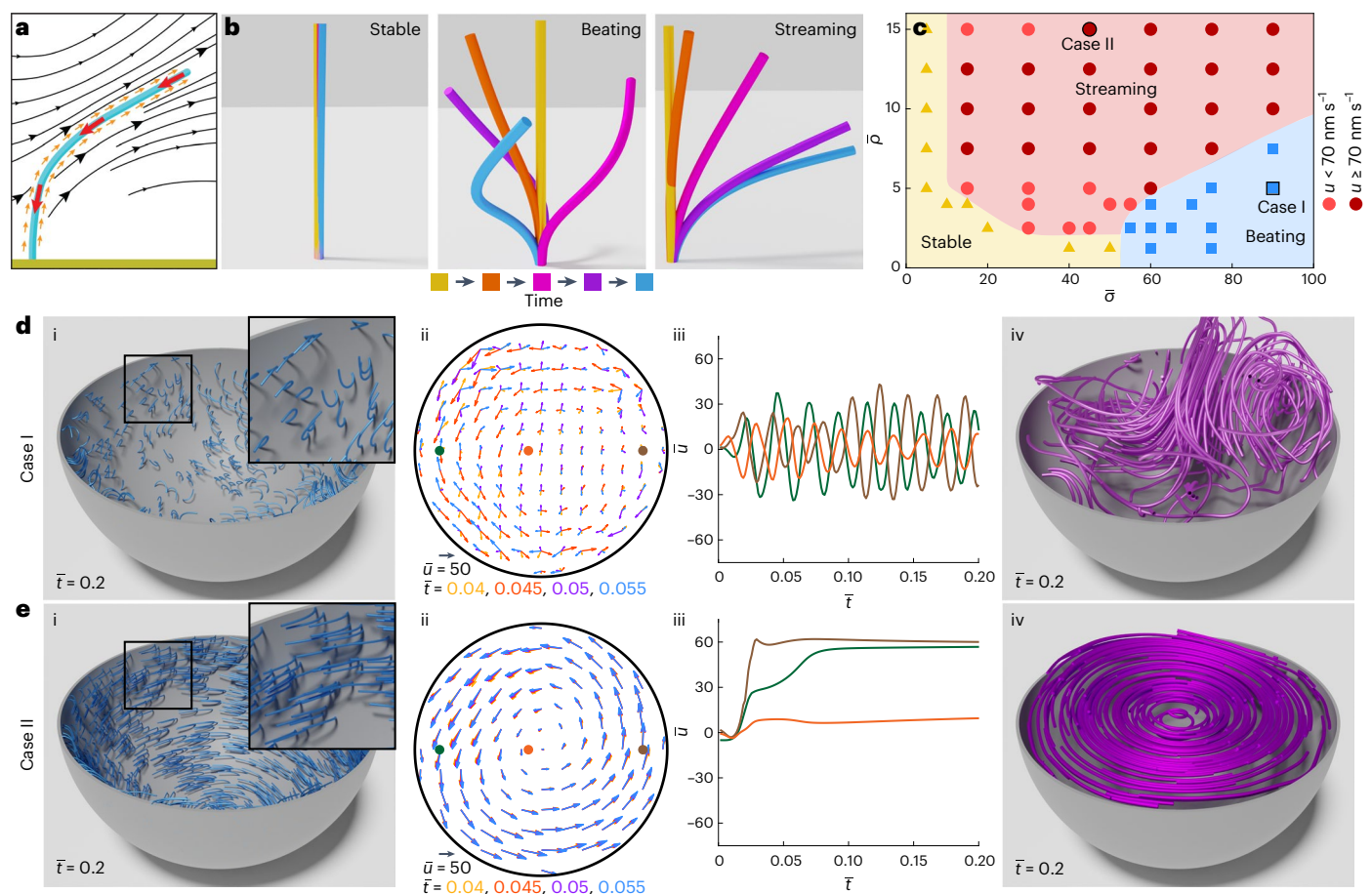
Fig. 1 | Hydrodynamic interactions of motor-loaded microtubules generate intracellular flows. a, Schematic illustrating a microtubule (blue) anchored normal to the cell surface (green) subject to active forcing and immersed in a viscous Newtonian fluid (that is, cytoplasm). Large red arrows show compressive stress on the microtubule, small orange arrows represent stress on the fluid, and black lines indicate flows in the fluid. **b**, Three regimes of microtubule behaviour: stable regime with little microtubule deformation (left), beating regime with microtubules oscillating (middle, case I) and the streaming regime with microtubules (collectively) bending (right, case II). Microtubule colours represent time evolution. **c**, Within a spherical cell, the phase diagram of microtubule behaviours as a function of adimensional microtubule areal density

$\bar{\rho}$ and motor forces $\bar{\sigma}$. The regions in yellow, red, and blue represent stable, streaming and oscillation phases, respectively. The colour of the red circles represents the characteristic streaming speed (flow speed at a distance $0.8\,R$ from the centre). The case I data point has $\bar{\rho} = 5$ and $\bar{\sigma} = 90$, and case II has $\bar{\rho} = 15$ and $\bar{\sigma} = 45$. **d**,**e**, For cases I (**d**) and II (**e**), cut-away view of instantaneous microtubule configurations in the spherical cell (i), 2D projection of velocity field in the sectioning equatorial plane at four time points (ii), the adimensional azimuthal velocity component $\bar{u}$ at the three points in the equatorial plane as a function of adimensional time $\bar{t}$ (iii) and 3D streamlines integrated from the 3D velocity field (iv). Curve colours correspond to the coloured point in preceding velocity plots.

Later, typically in stage 10b, when the oocyte is 150–300 µm long and 100–200 µm wide, large-scale streaming arises, often appearing as a vortex and having a typical speed of 100–400 nm s⁻¹ (refs. 17–19). This vortex was proposed to be generated by beds of flexible microtubules anchored to the actomyosin cortex, serving as tracks for plus-end-directed kinesin-1 motor proteins moving free microtubules and other payloads through an apparently viscous ooplasm[18–23]. One simulated model of ~100 motor-loaded, flexible microtubules above a no-slip plane showed emergence of ordered flow states reminiscent of observations during streaming[18]. More recently, an active and deformable porous-medium model was derived and used to argue that coherent vortical flows hundreds of microns in size can self-organize by means of the fluid-mediated coupling of active and flexible microtubules[24]. Parametric analysis of special azimuthally homogeneous solutions in a two-dimensional (2D) disk geometry identified a regime in which all microtubules coherently bend because of motor activity, resulting in a large-scale vortical flow. Although the model supports the idea of self-amplifying feedback generating large-scale flows, it remains to determine whether and how this mechanism works in more realistic three-dimensional (3D) geometries

where homogeneous solutions are not allowed and when other simplifying features of the model are removed. We present a computational approach that allows us to address these questions while making new and testable experimental predictions about the 3D structure of cytoplasmic flows.

Modelling hydrodynamically coupled motor-driven fibres

Conceptually, plus-end directed motors—here, kinesin-1—bind along anchored microtubules, carrying cargos towards free plus-ends and detaching once they reach there. Although the cargos seem varied, possibly including cellular organelles and yolk granules, free microtubules have been identified as one cargo crucial for robust streaming[19]. Given the lack of data on the details of cargo binding and payload densities and sizes, we assume the simplest model and, as in ref. 24, coarse-grain the forces of plus-end directed cargos on bound microtubules to a uniform compressive force density (that is, directed along the bound microtubule towards its anchored end) (Fig. 1a). An equal and opposite force is exerted on the surrounding fluid, thus satisfying Newton's Third Law. We find this is sufficient to recover

many aspects of observed streaming and to make several predictions for experiment.

Hence, consider N microtubules clamped to the inner surface of a spheroidal cell of effective radius R and surface area S ($\sim R^2$). Microtubules are well modelled as inextensible elastic slender bodies (ϵ = microtubule radius/length $\approx 10^{-3} \ll 1$) (refs. [25],[26]), and the cytoplasm is modelled as a Newtonian fluid of viscosity μ (ref. [22]). The shape of microtubule i at time t is given by $\mathbf{X}^i(s, t)$, where $0 \le s \le L^i$, with s the arclength from its base and L^i its length. Microtubule shape evolution caused by drag forces balancing elastic and motor forces is given by local slender-body theory[27–29]

$$\eta \left(\mathbf{X}_t^i - \bar{\mathbf{u}}^i(\mathbf{X}^i) \right) = (\mathbf{I} + \mathbf{X}_s^i \mathbf{X}_s^i)(\mathbf{f}^i - \sigma \mathbf{X}_s^i), \qquad (1)$$

where $\mathbf{X}_s^i = \partial_s \mathbf{X}^i$ is the microtubule unit tangent vector and $\eta = 8\pi\mu/c(\epsilon)$ is a drag coefficient having $c = |\ln e\epsilon^2|$ (given the logarithm, changes in ϵ enter very weakly). The velocity $\bar{\mathbf{u}}^i$ is that induced by all other microtubules and backflow from the cortex. The force density $\mathbf{f}^i = -E\mathbf{X}_{ssss}^i + (T^i\mathbf{X}_s^i)_s$ is the elastic force due to microtubule bending, with rigidity E and tensile forces, with tension T^i enforcing inextensibility. The microtubule-aligned term $-\sigma \mathbf{X}_s^i$ is the coarse-grained compressive load ($\sigma > 0$) exerted by kinesin-cargo complexes.

Given the background fluid velocity, equation (1) describes an initial value problem for microtubule shape. The background cytoplasmic velocity $\mathbf{u}(\mathbf{x})$, induced by all microtubules and by periphery backflow, satisfies the forced Stokes equation

$$\nabla p - \mu\Delta\mathbf{u} = \sum_{i=1}^N \int_0^{L^i} \mathrm{d}s\, \mathbf{f}^i(s)\delta(\mathbf{x} - \mathbf{X}^i(s)); \nabla \cdot \mathbf{u} = 0, \qquad (2)$$

where p is the pressure and no-slip is taken on the cortex. The minus ends of microtubules are pinned and clamped (respectively, $\mathbf{X}(0, t) = \mathbf{X}(0, 0)$ and $\mathbf{X}_s(0, t) = -\mathbf{n}(\mathbf{X}(0, t))$ with $\mathbf{n}$ the outward surface unit normal) at the cortex and the free plus end taken as torque and force free. That motor forces do not show up directly in determining the background velocity reflects their subdominant dipolar nature and the assumed close proximity of payloads to the load-bearing microtubules.

Equations (1) and (2) reflect a multiscale structure, with equation (1) evolving individual microtubules moving in a background flow created, by means of equation (2), by the collective forcing of the microtubule ensemble. Beds of motile cilia, also a multiscale active polymer transport system, are much studied for their capacity to self-organize, including through hydrodynamic interactions, into metachronal waves[30],[31]. Unlike the system studied here, cilia are internally actuated by dynein motors moving on ciliary microtubule doublets with fluid motion created directly by ciliary motion. Not so here, where even a single stationary and straight clamped microtubule will produce an upward cytoplasmic flow around it as a consequence of the payloads moving up on it, as conceptualized by equations (1) and (2).

Control parameters and numerical approach

The parameters in the model combine to yield three important timescales. Letting L be a characteristic microtubule length, from equation (1) come $\tau_r = \eta L^4/E$, the relaxation time of a single microtubule, and $\tau_m = L\eta/\sigma$, the time for motor forces to move a microtubule its own length. Equation (2) yields a second, faster microtubule relaxation time arising from collective hydrodynamic interactions, $\tau_c = \tau_r/\bar\rho$, where $\bar\rho = 8\pi NL^2/cS$ is the effective areal density of microtubules[24]. Ratios of these timescales determine the two dimensionless parameters dependent on the biophysical properties of microtubules and motors and their numbers: the dimensionless microtubule areal density $\bar\rho = \tau_r/\tau_c$, already introduced, and the dimensionless motor force $\bar\sigma = \tau_r/\tau_m = \sigma L^3/E$. The model has only two other, geometric, param-eters: the ratio of microtubule length to system size, $\delta = L/R$, and ϵ (entering weakly). Here we keep δ and ϵ constant, and thus $\bar\rho$ and $\bar\sigma$ govern the behaviour of the system.

Simulating this system efficiently for thousands of microtubules has peculiar challenges. The microtubules make the system geometry very complex, whereas their shape evolution is stiff because of their elasticity. Although the number of degrees of freedom—mainly dis-cretized microtubule forces and shapes—is not extreme ($\sim 10^{5-6}$), all are globally coupled by the Stokes equations, and the system needs to be simulated for long times. For this, we developed a fast and scalable computational platform that accurately evolves equations (1) and (2). It has three main components. First, boundary integral represen-tations and slender-body theory reduce the 3D Stokes equations in this complex domain to solving one-dimensional integrodifferential equations on microtubules and a coupled 2D integral equation on cell surfaces of nearly arbitrary geometry[29]. Second, a fast Stokes solver efficiently evaluates the non-local hydrodynamic interactions between microtubules and the periphery with linear scaling in the number of unknowns. Third, we use a stable implicit–explicit time-stepping scheme to efficiently evolve the stiff microtubule dynamics. This open source software is modular, allowing parallel computations across several nodes[32].

Self-organized regimes in a spherical cell

This infrastructure allows us to determine whether and how the behaviours predicted by the 2D analysis of the active porous-medium model survive in a fully 3D geometry that, for example, disallows homo-geneous solutions. Abstracting the stage 10 oocyte to a spherical cell of radius $R = 100$ μm and setting microtubule lengths to $L = 20$ μm (giving $\delta = 0.2$), we studied the model's long-time behaviour for various combinations of $\bar\rho$ and $\bar\sigma$. We use measured values of microtubule rigid-ity and cytoplasmic viscosity (Methods), giving a single microtubule relaxation time of $\tau_r = 16,000$ s (somewhat less than the 10 h duration of stage 10). Typically, we placed the microtubules at random statisti-cally uniform positions, achieving a given $\bar\rho$ with initial straight configurations normal to the surface. We found three basic behaviours: the cell's microtubules remaining nearly straight, its microtubules all beating near the same frequency or its microtubules bending collec-tively and remaining bent (Fig. 1b). On this basis, we grouped the simu-lations to map out domains of these qualitatively different behaviours (Fig. 1c). For low motor forces or low density, we find a stable phase where microtubules remain nearly straight (Fig. 1c, yellow). For larger motor forces and moderate microtubule density, we observed phases where microtubules periodically beat (Fig. 1c, blue). For a large range of parameters where microtubule density and motor strength are bal-anced, the model exhibits a streaming phase in which most microtubules bend collectively and remain bent (Fig. 1c, red). The emergence and structure of this phase is the principal theme of this work. Consistent with the prediction of the earlier coarse-grained analysis, the beating regime arises only beyond a critical motor force, and the streaming regime arises only above a critical microtubule density.

The microtubules' configurations and forces determine the instan-taneous 3D flow structure through equation (2). In the stable regime, there are local cytoplasmic flows near each microtubule but negligible flows inside the cell (Supplementary Fig. 1). For case I in the phase diagram (as Supplementary Video 1 makes clear), initially straight microtubules evolve into a beating state having dynamic regions of apparently synchronized beating (Fig. 1d(i) inset). Whether this cor-responds to a collective state as has been observed in models of ciliary beds[31],[33] is an interesting question that will be addressed quantitatively elsewhere. The associated internal velocity field is spatially complex and unsteady (Fig. 1d(ii) and Supplementary Video 2). Individual veloc-ity traces show a basic underlying frequency (for example, Fig. 1d(iii)) on the scale of τ_m, the motor time, at essentially the beat frequency of an isolated active microtubule, but with persistent relative phase drift.

The spatial complexity of these flows (Fig. 1d(iv)) shows the instantaneous streamlines within the cell. Perhaps coincidentally, the short-range spatial correlation is reminiscent of cytoplasmic seething in earlier development stages[21,34,35]. The emergence of oscillations of single driven filaments has been studied in related contexts: for example, refs. [36–38].

The streaming phase

Henceforth, we focus on the streaming phase (case II in the phase diagram), which generates flows similar to those typically observed in oogenesis stages 10b and beyond. In this region, we find that the initially straight microtubules at first bend in seemingly random directions. Gradually, these deformations align into an array of bent microtubules wrapping around an axis of symmetry (Fig. 1e(i) and Supplementary Video 3). This emergent axis is sensitive to details of initial data and microtubule patterning. The associated streaming flow is nearly steady, strongly vortical, fills the cell, has speeds ~100 nm s^{-1} and is reached rapidly on the order of τ_c, the collective relaxation timescale (Fig. 1e(ii–iv) and Supplementary Video 4).

Given that the streaming flow is essentially vortical about an extended axis, we refer to it as a twister. Setting the axis of the twister flow to $\hat{z}$ and examining its 3D streamlines shows the vortical component as indeed filling the cell and having a weaker swirl component (Fig. 2a,b) moving fluid inwards from the poles along the twister axis with a return flow outwards along the cell perimeter. That is, the secondary flow consists of two counter-rotating toroidal vortices, one in each hemisphere, wrapped around the twister axis. The simulated streaming flows can be well fit away from the boundaries as a flow with surface slip by superposing a purely 2D rotational flow with an aligned axisymmetric bitoroidal flow that satisfies the no-slip condition[39]. For case II, the strength of the rotational flow is ~20 times larger than the bitoroidal flow (Fig. 2b,c and Methods).

The dominant vortical flow arises from the collective bending of the majority of microtubules around a common axis (Fig. 1e(i)), whereas the swirl component arises from microtubule conformations around 'defect centres', our label for the points where the internal vortex axis ends at the cell surface. As a proxy for microtubule orientation and deformation, we define the microtubule surface polarity vector (Fig. 2d):

$$\mathbf{p}^i(t) = (\mathbf{I} - \mathbf{nn}) \cdot \frac{\mathbf{X}^i(L^i, t) - \mathbf{X}^i(0, t)}{L^i}, \text{ giving that } |\mathbf{p}^i| \leq 1. \quad (3)$$

Microtubules near defect centres are relatively straight (that is, have low $|\mathbf{p}^i|$), as the flow direction becomes indeterminate there (Fig. 2e). In these defect regions, the $\mathbf{p}$ field shows an inwardly oriented spiral pattern (Fig. 2f) consistent with the rotational flow and the pumping of cytoplasm that pulls fluid in peripherally. Self-consistently, payloads moving on these microtubules produce a tangential secondary flow towards the defect, and incompressibility yields both the inward axial flow and the global return flow. In the language of liquid-crystal physics, the polarity field structure is a combination of two +1-order disclination singularities.

The twisters we find here are cell-spanning, 3D flow states. This has consequences for their observation by means of microscopy, which typically images 2D cross-sections slicing through the cell (although confocal z-stacks may give some 3D structure). One then expects that the flows thus imaged will be in planar cross-sections set at some random angle relative to the twister axis. This is illustrated in Fig. 2g–i, which, by sampling in differently angled planes through the cell, shows a full vortex, an apparently displaced and distorted one and a fully transverse streaming flow. These are nonetheless all images of the same flow state.

Live imaging of cytoplasmic flows and cortical microtubules

A central feature of our model is that the flow near the cell surface is locally set by the orientation of the microtubules (Fig. 3a).
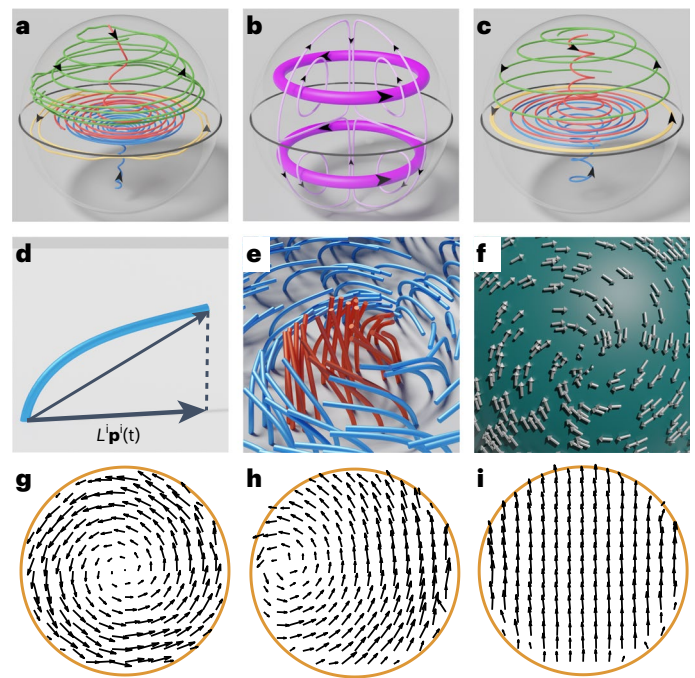

Fig. 2 | Twisters are a combination of a strong vortical flow and a weak bitoroidal flow. a, Streamlines from a simulation of case II ($\bar{\rho} = 15$, $\bar{\sigma} = 45$) in the streaming region. Streamlines starting near the equatorial plane remain there for long times, showing nearly circular paths (yellow). Streamlines starting near the poles move inwards on a spiral path towards the equatorial plane and then expand towards the periphery (red and blue). Streamlines starting above (or below) the equatorial plane near the cell periphery show the return flow back towards the pole (green). **b**, Streamlines from two simple solutions to the Stokes equations inside a sphere: a strong 2D constant vorticity flow (thick streamlines) and a weaker bitoroidal flow (thin streamlines). Both velocity fields are tangent to the confining sphere. **c**, Streamlines from best-fit combination of these two flows in approximating the flow in **a**. **d**, Schematic defining the microtubule of length L and polarity vector $\mathbf{p}$. The blue fibre represents the configuration of a microtubule anchored to the surface. The black vectors represent the end-to-end vector in 3D and its projection $\mathbf{p}$ on the surface. Note $|\mathbf{p}| \leq 1$. **e**, Microtubule configuration near the defect for simulation in **a**. Microtubules with polarity vectors satisfying $|\mathbf{p}| < 0.7$ (less bent) are coloured in red, and those with $|\mathbf{p}| \geq 0.7$ are coloured blue. **f**, View of the $|\mathbf{p}|$ distribution around the defect centre shown in **e** with low microtubule alignment. **g–i**, 2D projection of velocity fields from simulation in **a** in the sectioning equatorial planes when the plane normal is aligned with the z axis (**g**), has angle π/4 relative to the z axis (**h**) and is perpendicular to the z axis (**i**).

Moreover, because the flow is generated by motors moving along the microtubules, the flow speed increases from the centre of the vortex towards the microtubule bed and then diminishes near the cell surface because of the no-slip boundary condition (Fig. 3b). We successfully tested both of these predictions in live *Drosophila* oocytes (Supplementary Video 5). We performed particle imaging velocimetry (PIV) using endogenous particles (probably yolk granules and other particles) as flow tracers. To accurately measure the 3D cytoplasmic flow field both in the interior and near the oocyte cortex, we used overset grids, which combine square grids in the interior of the oocytes with surface-conforming grids near the cortex derived from its local geometry (Fig. 3c, Methods and Supplementary Fig. 2). We often observed a vortical flow spanning ~100 μm, with characteristic flow speeds of 100–300 nm s^{-1} (Fig. 3d, Supplementary Fig. 3). Our flow measurements are similar to previous studies[15,40] and comparable with the walking speed of kinesin-1 (~200–500 nm s^{-1}) (refs. [18,19,41,42]). Consistent with modelling predictions, the speed
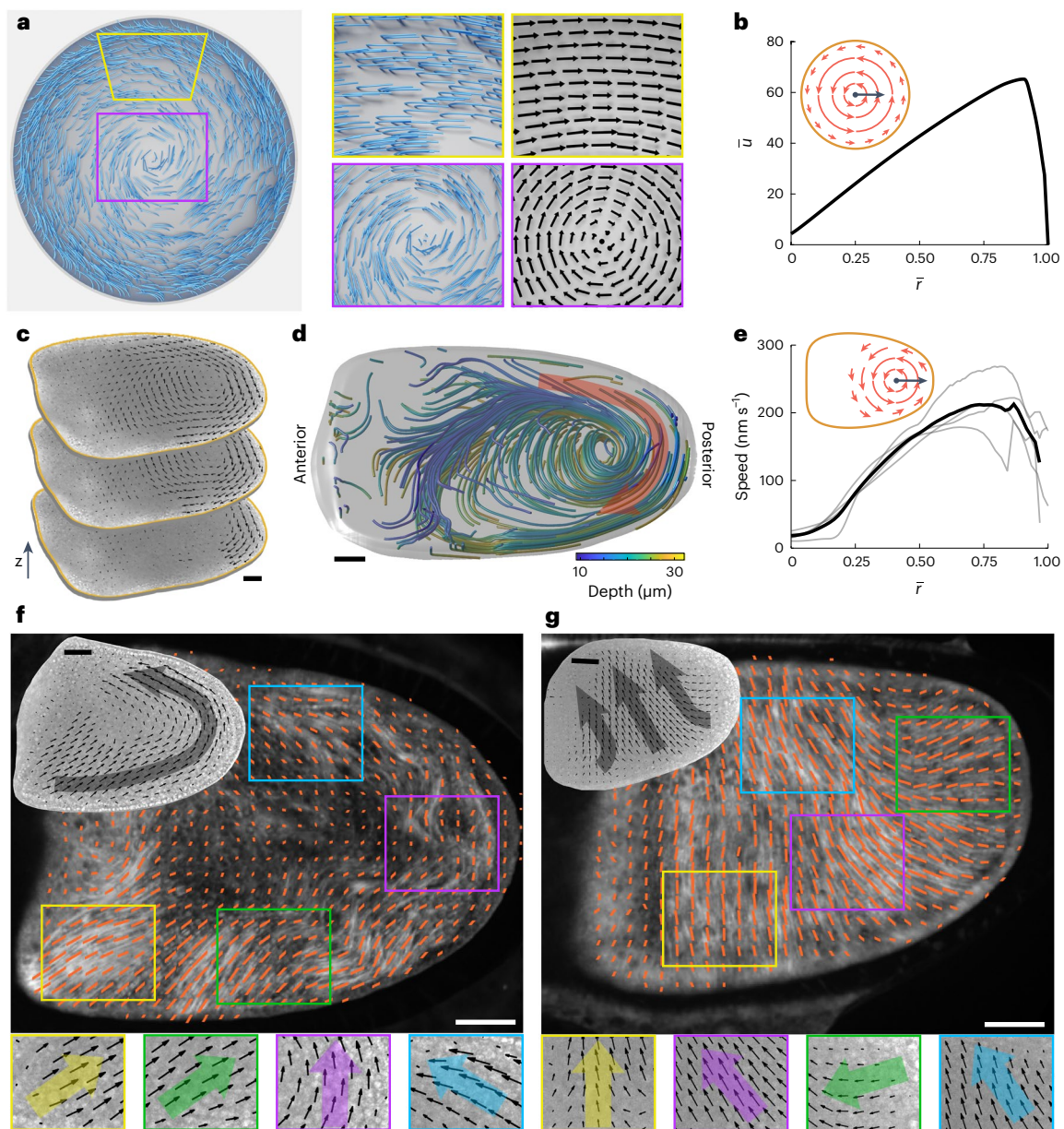
Fig. 3 | Surface microtubule orientation and cytoplasmic velocity fields.
a, Microtubule configurations at steady state from a simulation on a sphere from case II ($\bar{p} = 15$, $\bar{\sigma} = 45$) in the streaming region (left) and selected regions from the same snapshot with corresponding velocity fields in the vicinity of the surface (right). **b**, Adimensional speed $\bar{u}$ as a function of normalized distance $\bar{r} = r/R$ from the vortex centre in a cross-section (inset) for simulation in **a**. **c**, 2D velocity field in an oocyte measured by overset grid particle image velocimetry. Arrows show the direction and relative magnitude of the velocity. Measurements were done at consecutive z-sections from the oocyte surface. Alignment of the anterior–posterior axis parallel to the imaging plane is a natural consequence of mounting the oocyte for microscopy. Scale bar, 25 µm. **d**, Computed 3D streamlines near the oocyte surface from the reconstructed velocity field. Colour indicates depth; red arrow shows the flow direction. Although the planar projection of the flow spirals inwards, flows along the vortical axis maintain 3D incompressibility (Fig. 2a–c). Scale bar, 25 µm. **e**, Flow speed as a function of normalized distance $\bar{r}$ from the vortex centre (inset) measured in oocytes. Here, $\bar{r} = r/r_0$, where r_0 is the shortest distance from the vortex centre to the periphery. Grey lines indicate measurements from four different oocytes, and the black line shows their average. **f**,**g**, Large panels: near-surface microtubules in oocytes imaged in maternally derived GFP-αtub *Drosophila*. Orange lines represent microtubules' local orientation, with length representing the local degree of microtubule alignment measured by Gabor filter response. Upper left insets: the cytoplasmic velocity field (black arrows) measured by PIV in the same oocyte in a plane 15 µm from the surface. Lower boxes: cytoplasmic velocity fields for corresponding labelled regions. Coloured arrows therein are average microtubule orientation in the corresponding regions. Scale bars, 25 µm.

of cytoplasmic flow increased from the centre of the vortex towards the oocyte periphery and sharply decreased near the cortex (Fig. 3e). The measured flow speed (100–300 nm s^{-1}) is comparable to simulations (~100 nm s^{-1}). We measured the local microtubule orientation in confocal fluorescent images of oocytes expressing green fluorescent protein (GFP)-tagged α-tubulin (Fig. 3f,g, Supplementary Fig. 4 and Methods). In agreement with the model, the local cytoplasmic velocity field in oocytes is well aligned with the orientation field of cortical microtubules (Fig. 3f,g).

These two flow reconstructions, which show a distorted vortical structure and transverse streaming, and Fig. 3d, which shows a clear vortex, illustrate the variety of flows observed through live imaging. They are consistent with Fig. 2g–i as image slices through a basic twister structure.
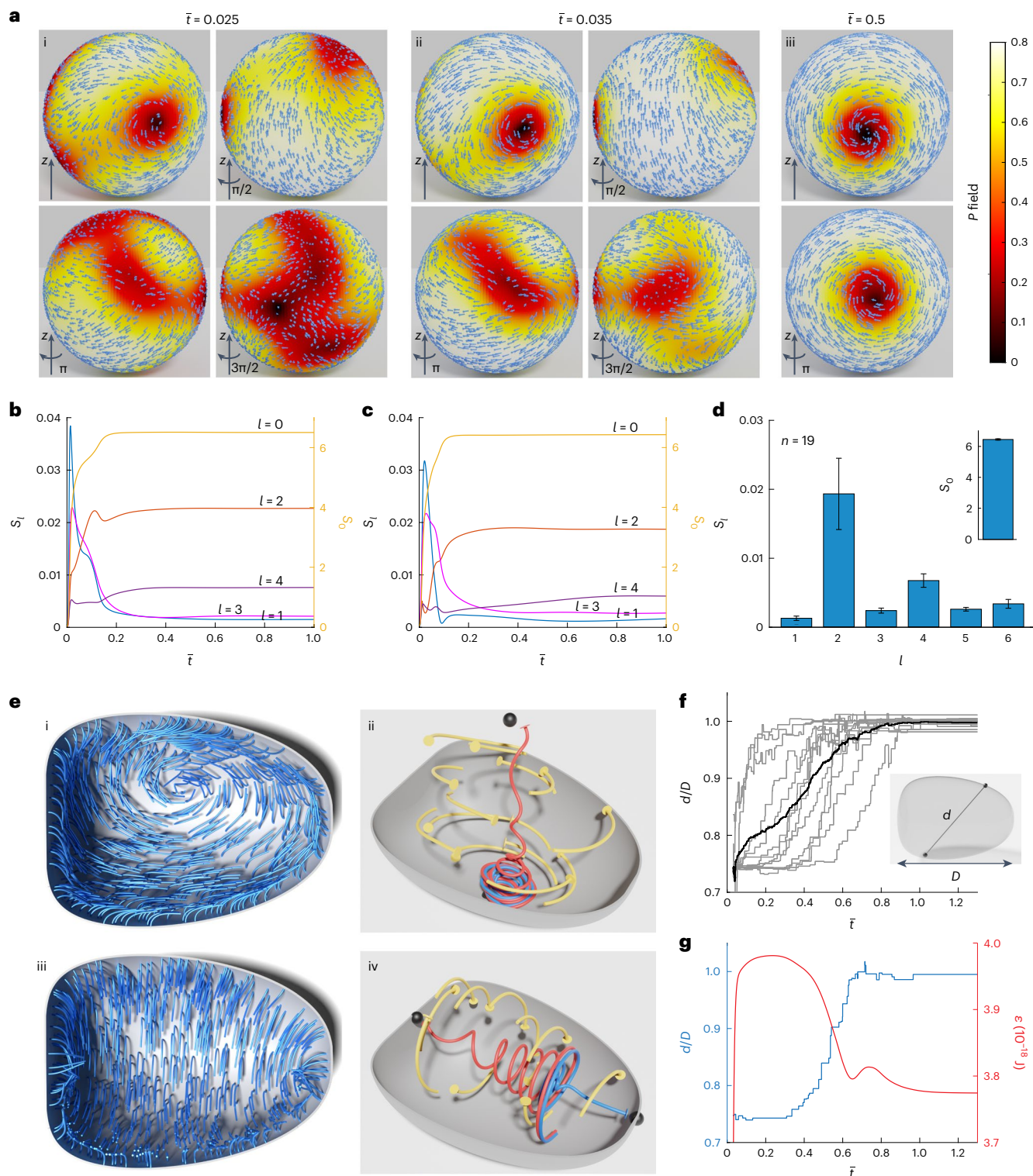
Fig. 4 | The structure of the streaming flow is robust. a, Microtubule surface polarity vectors $\mathbf{p}^i$ (shown as arrows) and the scalar polar order parameter P from several views from a simulation of case II ($\bar{\rho} = 15$, $\bar{\sigma} = 45$). Views (i) and (ii) are at early time ($\bar{t} = 0.025$, $\bar{t} = 0.035$) and (iii) at long time ($\bar{t} = 0.5$). $P \approx 1$ (bright) represents a high level of local alignment, and $P \approx 0$ (dark) represents a lack of local alignment. **b**, Angular power of spherical harmonic coefficients $\tilde{P}_{lm}$ of the P field corresponding to degree l, $s_l(t) = \sum_{m=-l}^{m=l} |\tilde{P}_{lm}(t)|^2/(2l+1)$, $l \geq 0$, for a simulation whose microtubules have initially bent conformations. **c**, Angular power for a second simulation having identical microtubule anchoring points as in **b**, but with differently bent initial conformations. The right and left axes represent $l = 0$ and $l \neq 0$, respectively. **d**, Bar graph representing the mean steady-state value of s_l ($l = 0$, inset) for $n = 19$ such simulations. Error bars show standard deviation.

Similar statistics are found by sampling different microtubule anchoring distributions (Supplementary Fig. 5). **e**, Microtubule configurations from a simulation with cell geometry similar to *Drosophila* oocyte from an early (i) and a late (iii) time point, using control parameters of case II ($\bar{\rho} = 15$, $\bar{\sigma} = 45$). Streamlines of the instantaneous flow field at the corresponding times (ii, iv). The disks represent the point of origin of the streamline. The streamlines in red and blue have points of origin near the regions with the lowest microtubule polarity P, denoted by black spheres. **f**, Distance between the two defect centres d normalized by oocyte length D as a function of time for 13 simulations in the oocyte geometry, as indicated in the inset (grey, individual simulations; black, average). **g**, Normalized distance between the defect centres (blue) and total elastic energy $\mathcal{E}$ of microtubules (red) as a function of time for simulation in **e**.

Robust emergence of twisters

We studied the emergent states over different initial conditions and for different realizations of statistically uniform placement of microtubules. This showed self-organized streaming to be very robust, with the main variation being the orientation of the twister in the cell (Methods and Supplementary Note 1).

The evolution towards this state can be followed through the dynamics of a surface polar order parameter $P(\mathbf{y})$ ($\mathbf{y}$ on the surface) of microtubules obtained by averaging surface polarity vectors over a (sliding) surface disk v centred on $\mathbf{y}$: $P = |\mathbf{P}|$, where $\mathbf{P}(\mathbf{y},t) = \langle \mathbf{p}^i(t) \rangle_v$. Low polar order is achieved by cancellation of anti-aligned $\mathbf{p}^i$ vectors or by their originating microtubules being close to orthogonal to the surface (both of which are evinced near defect centres; Fig. 2e,f). For initially straight microtubule beds, $P(\mathbf{y}, t=0) \equiv 0$. This unstable state quickly evolves into a state with several spatially complex regions with high polar order (Fig. 4a and Supplementary Videos 6 and 7). Each of these high-order regions is contributing to the cytoplasmic flow through which these regions compete and interact. The low-order regions gradually sharpen as high-order regions expand and merge, finally resolving into the axisymmetric swirling state whose axis joins the two opposing defect centres of low polar order (Fig. 4a(ii,iii)).

Although the orientation of this axis depends on the fine-grained details of microtubule placement and initial conditions, the final flows and order parameter fields all evolve towards the same basic attractor. Their strikingly similar progression of self-organization towards the streaming twister state can be readily appreciated by examining the P field's angular power spectra: $s_l(t) = \sum_{m=-l}^{m=l} |\tilde{P}_{lm}(t)|^2/(2l+1)$ (components of the spherical harmonic power spectrum, with l the polar mode index). As the system evolves towards the twister state, both even and odd l modes initially grow and then either (1) saturate for even l while being dominated by the global $l = 0$ mode or (2) relax back to relatively small amplitudes for odd l modes. The relaxation timescale of these modes is similar to the collective relaxation timescale τ_c. We consistently observed similar dynamics and end states for simulations in which anchoring points or microtubule initial conditions were varied (Fig. 4b–d and Supplementary Fig. 5).

Model dynamics in an oocyte geometry

Like cows, oocytes actually have a variety of shapes: they are very roughly distended ellipsoids with approximate symmetry around their anterior–polar axis. How might cell nonsphericity affect twister formation and dynamics? To investigate this, we simulated motor-loaded microtubule beds anchored within an axisymmetric cell having a shape resembling stage 10b oocytes (Methods). The dynamics is first familiar and then surprising. Beginning from straight microtubules and using the case II values for $\bar{\sigma}$ and $\bar{\rho}$, the progressive growth and coarsening of domains with bent but aligned microtubules is again observed. This process leads again to a twister (Fig. 4e(i), Supplementary Fig. 8 and Supplementary Video 8) that sits askew in the cell, respecting no obvious geometric symmetry, with the structure of its interior flows a geometric perturbation of the rotational plus bitoroidal flows found in spheres (Fig. 4e(ii)). Evolving from different samples of microtubule anchoring points leads to twisters at differing orientations, usually tilted within the cell (Fig. 4f). However, we find that in all cases for this cell shape, the newly formed twisters slowly reorient into alignment with the anterior–posterior cell axis (Fig. 4e(iii),f) while preserving the basic interior flow structure (Fig. 4e(iv)). The reorientation observed in simulations occurs on the long timescale $\tau_r \approx 5$ h, consistent with observing vortices in vivo that are not aligned along the anterior-posterior axis.

What drives this reorientation? In this system, energy is stored in the elastic deformations of the microtubule bed measured by its total elastic energy

$$\mathcal{E}(t) = \sum_{i=1}^{N} \frac{E}{2} \int_0^{L^i} ds [\kappa^i(s,t)]^2, \tag{4}$$

where κ^i is microtubule curvature. The elastic energy is driven by motors performing work on the system and dissipated by viscous and drag forces. Although the energy is initially zero, as microtubules are initially straight, $\mathcal{E}$ begins a rapid rise as microtubules collectively bend and reaches its maximum as the twister forms (Fig. 4g). Rather than lingering there, as it would if the system were in a steady state, $\mathcal{E}$ immediately begins decreasing, and the twister axis starts its reorientation towards the anterior–posterior axis. Meanwhile, $\mathcal{E}$ generally decreases, and the system ultimately relaxes into a steady state of reduced elastic energy.

We note that experiments indicate a lower microtubule density in the posterior[43–45]. To investigate the effect of nonuniform microtubule distribution, we progressively diminished their density in the posterior and again found fast twister formation followed by slow reorientation (Supplementary Fig. 9 and Note 2).

Discussion

Taken together, our results underscore the robustness of cytoplasmic streaming that emerges from hydrodynamic interactions among cortically anchored microtubules loaded with cargo-carrying motors. Fine-tuning is not required; as long as microtubule density and motor activity are in the wide domain of parameters that corresponds to stable streaming, self-organization takes care of the rest, establishing a cell-spanning twister. Naming such vortices twisters begs comparison with the more familiar kind. Tornadoes are inertia dominated and have highly localized vortical cores, maintained by axial swirl, away from which flow velocities decay. Our zero-Reynolds-number twisters have velocities rising from the centre, a la solid-body rotation, and reflect a precise balance between active surface driving and viscous dissipation. Self-organized boundary-driven vortices have arisen in other active matter systems, such as confined suspensions of swimming bacteria[38].

Our model makes several interesting predictions. As discussed, our twister states are volumetric structures, which predicts that standard microscopy imaging should show a variety of flows depending on how the imaging volume intersects the flow structure. This is consistent with our own experimental observations. Further, our simulations are of statistically uniform microtubule beds in axisymmetric cell shapes. Thus, our twisters have no preferred direction of rotation with respect to axes of cell symmetry. Our experimental flow reconstructions likewise showed no evidence for rotational biases, clockwise or counterclockwise, with respect to the anterior–posterior cell axis (Supplementary Fig. 3c,d). Our simulations show small secondary streaming flows originating from defect centres. Although the rotational flow seems very robust, these secondary flows may not be, and they may be affected by various cellular inhomogeneities; as yet, our microscopy imaging volumes are insufficient to make a clear comparison. Very interestingly, simulated twisters in oocyte shapes show a slow reorientation—on the long τ_r timescale—towards the anterior–posterior axis. Although this is a challenging prediction to test, requiring long-time, stable imaging of the oocyte, we are pursuing new observations. The nature of these dynamics also indicates the existence of manifold twister states towards which the system is rapidly attracted and on which twisters slowly move towards axis alignment, which we believe to be the state of minimum energy (supplementary Fig. 7a). This picture is consistent with simulations in spheres, where elastic energy also shows rapid peaking and then decay (Supplementary Fig. 7b). But the apparent overshoot is now far smaller, with subsequent dissipation towards a state of barely different energy (Supplementary Fig. 7a), indicating a slow twister dynamics driven by statistical details of microtubule placement rather than cell shape. The nature of transition to swirling and axis alignment requires further exploration, but it is interesting to note that changes

in viscosity (such as may occur on dissolution of the cellular actin meshwork[34,35]) do not, in our model, lead to state bifurcations but only change the timescale on which dynamics occurs.

What function might a twister serve? Before the onset of streaming, diffusion and motor-driven transport are the main means by which different classes of RNAs are transported and anchored to the the anterior, dorsal and posterior regions of the oocyte. Importantly, several gene products guard the oocyte against precocious streaming because it would interfere with the localization of transcripts needed for embryonic patterning[15,46]. Once these factors are stably localized, the oocyte switches to a streaming strategy for intracellular transport. The appearance of streaming may reflect its role in the uptake of yolk, the main source of protein in the embryo. Yolk proteins arrive at the future egg cell by means of internalization after binding to a specific receptor that localizes to the oocyte plasma membrane shortly before streaming onset[47]. The streaming flow might be used to efficiently disperse of the arriving yolk throughout the ooplasm. This idea is consistent with the fact that yolk proteins are known cargoes of kinesin-1 motors walking on cortically anchored microtubules[19] and with our preliminary analyses of the mixing capabilities of self-organized intracellular twisters.

Online content

Any methods, additional references, Nature Portfolio reporting summaries, source data, extended data, supplementary information, acknowledgements, peer review information; details of author contributions and competing interests; and statements of data and code availability are available at https://doi.org/10.1038/s41567-023-02372-1.

References

1. Corti, B. *Osservazioni microscopiche sulla tremella e sulla circolazione del fluido in una pianta acquajuola* (Rocchi, 1774).
2. Yi, K. et al. Dynamic maintenance of asymmetric meiotic spindle position through Arp2/3-complex-driven cytoplasmic streaming in mouse oocytes. *Nat. Cell Biol.* **13**, 1252–1258 (2011).
3. Almonacid, M. et al. Active diffusion positions the nucleus in mouse oocytes. *Nat. Cell Biol.* **17**, 470–479 (2015).
4. Deneke, V. E. et al. Self-organized nuclear positioning synchronizes the cell cycle in *Drosophila* embryos. *Cell* **177**, 925–941 (2019).
5. Glotzer, J. B., Saffrich, R., Glotzer, M. & Ephrussi, A. Cytoplasmic flows localize injected oskar RNA in *Drosophila* oocytes. *Curr. Biol.* **7**, 326–337 (1997).
6. van de Meent, J.-W., Tuval, I. & Goldstein, R. E. Nature's microfluidic transporter: rotational cytoplasmic streaming at high Péclet numbers. *Phys. Rev. Lett.* **101**, 178102 (2008).
7. Hird, S. N. & White, J. G. Cortical and cytoplasmic flow polarity in early embryonic cells of *Caenorhabditis elegans*. *J. Cell Biol.* **121**, 1343–1355 (1993).
8. Emmons, S. et al. Cappuccino, a *Drosophila* maternal effect gene required for polarity of the egg and embryo, is related to the vertebrate limb deformity locus. *Genes Dev.* **9**, 2482–2494 (1995).
9. Trong, P. K., Doerflinger, H., Dunkel, J., St Johnston, D. & Goldstein, R. E. Cortical microtubule nucleation can organise the cytoskeleton of *Drosophila* oocytes to define the anteroposterior axis. *eLife* **4**, e06088 (2015).
10. Gross, P. et al. Guiding self-organized pattern formation in cell polarity establishment. *Nat. Phys.* **15**, 293–300 (2019).
11. Goldstein, R. E. & van de Meent, J.-W. A physical perspective on cytoplasmic streaming. *Interface Focus* **5**, 20150030 (2015).
12. Lu, W. & Gelfand, V. I. Go with the flow–bulk transport by molecular motors. *J. Cell Sci.* **136**, jcs260300 (2023).
13. Shamipour, S., Caballero-Mancebo, S. & Heisenberg, C.-P. Cytoplasm's got moves. *Dev. Cell* **56**, 213–226 (2021).
14. Woodhouse, F. G. & Goldstein, R. E. Cytoplasmic streaming in plant cells emerges naturally by microfilament self-organization. *Proc. Natl Acad. Sci.* **110**, 14132–14137 (2013).
15. Quinlan, M. E. Cytoplasmic streaming in the *Drosophila* oocyte. *Annu. Rev. Cell Dev. Biol.* **32**, 173–195 (2016).
16. Becalska, A. N. & Gavis, E. R. Lighting up mRNA localization in *Drosophila* oogenesis. *Development* **136**, 2493–2503 (2009).
17. Gutzeit, H. & Koppa, R. Time-lapse film analysis of cytoplasmic streaming during late oogenesis of *Drosophila*. *Development* **67**, 101–111 (1982).
18. Monteith, C. E. et al. A mechanism for cytoplasmic streaming: kinesin-driven alignment of microtubules and fast fluid flows. *Biophys. J.* **110**, 2053–2065 (2016).
19. Lu, W., Winding, M., Lakonishok, M., Wildonger, J. & Gelfand, V. I. Microtubule–microtubule sliding by kinesin-1 is essential for normal cytoplasmic streaming in *Drosophila* oocytes. *Proc. Natl Acad. Sci.* **113**, E4995–E5004 (2016).
20. Palacios, I. M. & Johnston, D. S. Kinesin light chain-independent function of the kinesin heavy chain in cytoplasmic streaming and posterior localization in the *Drosophila* oocyte. *Development* **129**, 5473–5485 (2002).
21. Serbus, L. R., Cha, B. J., Theurkauf, W. E. & Saxton, W. M. Dynein and the actin cytoskeleton control kinesin-driven cytoplasmic streaming in *Drosophila* oocytes. *Development* **132**, 3743–52 (2005).
22. Ganguly, S., Williams, L. S., Palacios, I. M. & Goldstein, R. E. Cytoplasmic streaming in *Drosophila* oocytes varies with kinesin activity and correlates with the microtubule cytoskeleton architecture. *Proc. Natl Acad. Sci. USA* **109**, 15109–15114 (2012).
23. Ravichandran, A. et al. Chronology of motor-mediated microtubule streaming. *eLife* **8**, e39694 (2019).
24. Stein, D. B., De Canio, G., Lauga, E., Shelley, M. J. & Goldstein, R. E. Swirling instability of the microtubule cytoskeleton. *Phys. Rev. Lett.* **126**, 028103 (2021).
25. Gittes, F., Mickey, B., Nettleton, J. & Howard, J. Flexural rigidity of microtubules and actin filaments measured from thermal fluctuations in shape. *J. Cell Biol.* **120**, 923–934 (1993).
26. Shelley, M. J. The dynamics of microtubule/motor-protein assemblies in biology and physics. *Annu. Rev. Fluid Mech.* **48**, 487–506 (2016).
27. Keller, J. B. & Rubinow, S. I. Slender-body theory for slow viscous flow. *J. Fluid Mech.* **75**, 705–714 (1976).
28. Tornberg, A.-K. & Shelley, M. J. Simulating the dynamics and interactions of flexible fibers in stokes flows. *J. Comput. Phys.* **196**, 8–40 (2004).
29. Nazockdast, E., Rahimian, A., Zorin, D. & Shelley, M. A fast platform for simulating semi-flexible fiber suspensions applied to cell mechanics. *J. Comput. Phys.* **329**, 173–209 (2017).
30. Elgeti, J. & Gompper, G. Emergence of metachronal waves in cilia arrays. *Proc. Natl Acad. Sci. USA* **110**, 4470–4475 (2013).
31. Chakrabarti, B., Fürthauer, S. & Shelley, M. J. A multiscale biophysical model gives quantized metachronal waves in a lattice of beating cilia. *Proc. Natl Acad. Sci. USA* **119**, e2113539119 (2022).
32. SkellySim cellular dynamics package. *GitHub* https://github.com/flatironinstitute/SkellySim (2023).
33. Kanale, A. V., Ling, F., Guo, H., Fürthauer, S. & Kanso, E. Spontaneous phase coordination and fluid pumping in model ciliary carpets. *Proc. Natl Acad. Sci.* **119**, e2214413119 (2022).
34. Theurkauf, W. E. Premature microtubule-dependent cytoplasmic streaming in cappuccino and spire mutant oocytes. *Science* **265**, 2093–2096 (1994).
35. Dahlgaard, K., Raposo, A. A., Niccoli, T. & St Johnston, D. Capu and Spire assemble a cytoplasmic actin mesh that maintains microtubule organization in the *Drosophila* oocyte. *Dev. Cell* **13**, 539–553 (2007).

36. Isele-Holder, R. E., Jäger, J., Saggiorato, G., Elgeti, J. & Gompper, G. Dynamics of self-propelled filaments pushing a load. *Soft Matter* **12**, 8495–8505 (2016).

37. De Canio, G., Lauga, E. & Goldstein, R. E. Spontaneous oscillations of elastic filaments induced by molecular motors. *J. R. Soc. Interface* **14**, 20170491 (2017).

38. Ling, F., Guo, H. & Kanso, E. Instability-driven oscillations of elastic microfilaments. *J. R. Soc. Interface* **15**, 20180594 (2018).

39. Stone, H., Nadim, A. & Strogatz, S. H. Chaotic streamlines inside drops immersed in steady stokes flows. *J. Fluid Mech.* **232**, 629–646 (1991).

40. Williams, L. S., Ganguly, S., Loiseau, P., Ng, B. F. & Palacios, I. M. The auto-inhibitory domain and ATP-independent microtubule-binding region of Kinesin heavy chain are major functional domains for transport in the *Drosophila* germline. *Development* **141**, 176–186 (2014).

41. Brendza, K. M., Rose, D. J., Gilbert, S. P. & Saxton, W. M. Lethal kinesin mutations reveal amino acids important for atpase activation and structural coupling. *J. Biol. Chem.* **274**, 31506–31514 (1999).

42. Loiseau, P., Davies, T., Williams, L. S., Mishima, M. & Palacios, I. M. *Drosophila* PAT1 is required for kinesin-1 to transport cargo and to maximize its motility. *Development* **137**, 2763–2772 (2010).

43. Theurkauf, W. E., Smiley, S., Wong, M. L. & Alberts, B. M. Reorganization of the cytoskeleton during *D*rosophila oogenesis: implications for axis specification and intercellular transport. *Development* **115**, 923–936 (1992).

44. Nashchekin, D., Fernandes, A. R. & St Johnston, D. Patronin/shot cortical foci assemble the noncentrosomal microtubule array that specifies the *Drosophila* anterior-posterior axis. *Dev. Cell* **38**, 61–72 (2016).

45. Lu, W. et al. Competition between kinesin-1 and myosin-v defines *Drosophila* posterior determination. *eLife* **9**, e54216 (2020).

46. Manseau, L. J. & Schüpbach, T. cappuccino and spire: two unique maternal-effect loci required for both the anteroposterior and dorsoventral patterns of the *Drosophila* embryo. *Genes Dev.* **3**, 1437–1452 (1989).

47. Schonbaum, C. P., Perrino, J. J. & Mahowald, A. P. Regulation of the vitellogenin receptor during *Drosophila* melanogaster oogenesis. *Mol. Biol. Cell* **11**, 511–521 (2000).

Methods

We briefly formulate our model and outline our method of simulation, the technical details of which appear in ref. 29. The approach combines slender-body theory and boundary integral methods for solving the Stokes equations. A publicly available and elaborated version of the underlying code, SkellySim, is available from ref. 32.

In broad strokes, we simultaneously solve the coupled equations of motion, equations (1) and (2) in the main text, for the fluid and immersed microtubules confined in the cellular volume Ω and clamped at the boundary Γ. Because of the linearity of the Stokes equations, we can write the fluid velocity at $\mathbf{x}$ in Ω as $\mathbf{u}(\mathbf{x}) = \mathbf{u}^{mt}(\mathbf{x}) + \mathbf{u}^{\Gamma}(\mathbf{x})$, with $\mathbf{u}^{mt}(\mathbf{x}) = \sum_i \mathbf{u}^i(\mathbf{x})$ the superposition of velocities induced by forces and conformations of each microtubule i and $\mathbf{u}^{\Gamma}(\mathbf{x})$ the consequent backflow velocity induced by the no-slip condition at the confining boundary Γ.

The velocities $\mathbf{u}^{mt}$ and $\mathbf{u}^{\Gamma}$ are expressed in terms of two fundamental solutions to the Stokes equations, the Stokeslet tensor G (a second-rank tensor) and the Stresslet $\mathcal{T}$ (a third-rank tensor):

$$G(\mathbf{x}) = \frac{1}{8\pi\mu} \frac{\mathbf{I} + \hat{\mathbf{x}}\hat{\mathbf{x}}}{|\mathbf{x}|}; \quad \mathcal{T}(\mathbf{x}) = \frac{-3}{4\pi\mu} \frac{\hat{\mathbf{x}}\hat{\mathbf{x}}\hat{\mathbf{x}}}{|\mathbf{x}|^2}. \quad (5)$$

$\hat{\mathbf{x}} = \mathbf{x}/|\mathbf{x}|$. Slender-body theory for the Stokes equations gives that, to leading (logarithmic) order in the slenderness ratio ϵ, the velocity induced by a microtubule is given as a line integral of the distribution of the Stokeslets along its centerline

$$\mathbf{u}^i(\mathbf{x}) = \int_0^{L^i} G(\mathbf{x} - \mathbf{r}^i(s'))\mathbf{f}^i(s')\mathrm{d}s', \quad (6)$$

where $\mathbf{f}^i$ is the internal elastic force that a microtubule exerts on the fluid (see main text).

The second contribution, $\mathbf{u}^{\Gamma}$, accounts for the no-slip condition taken on Γ and is expressed as a surface convolution of the Stresslet over Γ with an unknown density $\mathbf{q}$,

$$\mathbf{u}^{\Gamma}(\mathbf{x}) = \int_{\Gamma} \mathrm{d}S_y\, \mathbf{n}(\mathbf{y}) \cdot \mathcal{T}(\mathbf{r}) \cdot \mathbf{q}(\mathbf{x}), \quad (7)$$

where $\mathbf{r} = \mathbf{x} - \mathbf{y}$ and $\mathbf{n}$ is the outward unit normal vector to Γ. In the parlance of integral equations, this is a double-layer representation. In such a representation, taking the limit $\mathbf{x} \to \Gamma$ of equation (5) and applying the no-slip condition, $\mathbf{u} = 0$, generates a well-conditioned Fredholm integral equation of the second kind for $\mathbf{q}$:

$$-\frac{1}{2}\mathbf{q}(\mathbf{x}) + \int_{\Gamma} \mathrm{d}S_y \mathbf{n}(\mathbf{y}) \cdot \mathcal{T}(\mathbf{r}) \cdot \mathbf{q}(\mathbf{y})$$
$$+ \int_{\Gamma} \mathrm{d}S_y [\mathbf{n}(\mathbf{x})\mathbf{n}(\mathbf{y})] \cdot \mathbf{q}(\mathbf{y}) = -\mathbf{u}^{mt}(\mathbf{x}), \quad \mathbf{x} \in \Gamma. \quad (8)$$

Here, the last term of the right-hand side is added to complete the rank (that is, make it uniquely invertible) of the integral equation. This term does not change the velocity $\mathbf{u}^{\Gamma}$ but does fix a constant in the pressure field[29]. In equation (1) of the main text, the background velocity for microtubule i is given by $\bar{\mathbf{u}}^i(\mathbf{x}) = \sum_{j \neq i}\mathbf{u}^j(\mathbf{x})$: that is, the flows induced by all other microtubules. At each time, the unknown field to determine for microtubule i is its tension field T^i, which enforces inextensibility. This condition generates, through equation (1) of the main text, integrodifferential equations for all the tensions T^i. Solution of the coupled system for $(\mathbf{q}, T)$ allows calculation of the microtubule velocities $\mathbf{X}_t^i(s, t)$.

The integrodifferential operators along the centerlines of the microtubules are discretized using fourth-order finite differences. For the time stepping, we use an adaptive explicit/implicit backward time-stepping scheme, which maintains accuracy while removing high-order stability stiffness constraints from the bending term. This results in a dense linear system of equations that we solve using the generalized minimal residual method with block-diagonal preconditioners. We accelerate computing the hydrodynamic interactions using the fast multipole method[48]. The complexity per time step scales with the total number of discretization points on microtubules and the cell surface.

Biophysical and numerical parameters of simulations

Biophysical: In our simulations, we chose the length of all microtubules to be $L = 20\ \mu m$—on the longer side if growing from dynamical instability—with bending rigidity $E = 20\ pN\ \mu m^2$ (ref. 25). A microtubule diameter of $\sim$20 nm gives $\epsilon \approx 5 \times 10^{-4}$. If the cell is spherical, it is of radius $R = 100\ \mu m$, taken in this abstracted shape as the typical size for stage 10 *Drosophila* oocytes. For an 'oocyte'-shaped cell, whose construction is described below, the length is 150 μm and width 108 μm. The immersing fluid is taken as Newtonian with viscosity $\mu = 1\ Pa\ s$ (ref. 22).

The relaxation time of a microtubule is estimated as $\tau_r = \eta L^4/E \approx 16{,}000$ s. For comparison, this is somewhat less than the duration of stage 10 of *Drosophila* development—about 10 h = 36,000 s—where large-scale streaming flows first appear. We note that streaming persists into stage 12. Generally we have $(\tau_c, \tau_m) = (\tau_r/\bar{\rho}, \tau_r/\bar{\sigma})$. For beating case I, this gives $(\tau_c, \tau_m) \approx (3{,}200, 180)$ s, whereas for the streaming case II, we have $(\tau_c, \tau_m) \approx (1{,}066, 355)$ s. The maximum allowable time step is $\Delta t = 0.16$ s, much smaller than any of faster timescales τ_c and τ_m.

Constructing anchoring sets and initial conditions of simulations

We set up simulations as follows. For a given cell geometry, microtubules are clamped orthogonally to the inner surface and each discretized with 64 points. The surface anchoring points are chosen randomly and have a uniform probability per unit area. These placements are then filtered to ensure that no two microtubules are closer than the distance $\Delta = 0.1L$ from each other. The initial shapes of the microtubules are typically set as straight lines but sometimes as curved lines produced as follows. We evolve the system forward, using initially straight microtubules, under the induced flow of 500 rotlets (point torque sources for the Stokes equations) randomly placed uniformly within the cell at a maximum distance of 0.78R from the centre. For the simulations in Fig. 4b–d and Supplementary Fig. 6c,d, the torque in each dimension is taken from a uniform distribution between [−5,5] pN μm. For the simulations in supplementary Fig. 6e, the torque in each dimension is taken from a uniform distribution between [−5ϵ,5ϵ] pN μm, where ϵ is varied between 0 and 0.1. $\epsilon = 0$ corresponds to the straight microtubule case and serves as a reference condition. These rotlets generate local flows that deform microtubules from their straight shapes, with the degree of deformation in the latter case controlled by ϵ. The rotlets are removed from the system after $t = 1.25 \times 10^{-4}\tau_r$, and the resulting microtubule configurations are used as initial data for further simulations.

Classification of microtubule dynamics in simulations

We established the phase diagram of the model on the basis of the dynamics and shapes of the microtubules in long-term simulations. In the stable phase, microtubules remain unperturbed and normal to the surface; in the beating phase, microtubules' shapes continuously change with time; in the streaming phase, microtubules attain steady deformed shapes. To classify the simulations into these three phases, we first measured the normalized positional variance of the microtubule's free end

$$\delta_i^2 = \frac{\left\langle \left(\mathbf{X}^i(L) - \langle \mathbf{X}^i(L)\rangle\right)^2 \right\rangle}{L^2}, \quad (9)$$

where the averaging is over a period of $\Delta t = 10^{-3}\tau_r$. If $\delta_i^2 < 0.1$, we consider the microtubule shape time-independent; otherwise, its shape is dynamic. For a simulation, if more than 90% of microtubules are

dynamic, we classify it as the beating phase; otherwise, it belongs to the stable or streaming phase. To distinguish between these two phases, we measured the projection of the microtubule end-to-end vector as

$$a^i = 1 - \hat{\mathbf{n}} \cdot \frac{\mathbf{X}^i(L) - \mathbf{X}^i(0)}{|\mathbf{X}^i(L) - \mathbf{X}^i(0)|}. \tag{10}$$

If $a^i < 0.05$, the microtubule is considered normal to the surface; otherwise, it is deformed. For a simulation, if more than 90% of microtubules are normal to the surface, we classify it as the stable phase. Otherwise, we classify it as the streaming phase.

Analytical approximation of the streaming flow in a sphere

We approximated the flow in simulations of the sphere as a superposition of a swirling flow $\mathbf{u}_s$ and an axisymmetric bitoroidal flow $\mathbf{u}_t$ (ref. 39),

$$\mathbf{u}_{ana} = \mathbf{u}_s + \mathbf{u}_t$$

$$\mathbf{u}_s(r, \theta, \phi) = \Omega \frac{r}{R} \sin(\theta) \hat{\boldsymbol{\phi}}$$

$$\mathbf{u}_t(r, \theta, \phi) = \frac{A}{R^3} \left[r(r^2 - W^2)(1 - 3\cos^2\theta)\hat{\mathbf{r}} + r(5r^2 - W^2)\cos(\theta)\sin(\theta)\hat{\boldsymbol{\theta}} \right], \tag{11}$$

where r, θ and ϕ are the radial, polar and azimuthal coordinates in the sphere and $\hat{\mathbf{r}}$, $\hat{\boldsymbol{\theta}}$ and $\hat{\boldsymbol{\phi}}$ are the unit vectors in the respective directions. The three parameters of the model are Ω, the strength of the swirling flow, A, the strength of the bitoroidal flow, and W, the radius associated with the bitoroidal flow. We fit our simulations of spherical geometry to this flow by minimizing $\xi = \int (\mathbf{u}_{ana} - \mathbf{u}_{sim})^2 \mathrm{d}V$, where the integration is over the sphere volume. For the minimization, we use the gradient descent algorithm for six free parameters, including three angles, to align the axis of the flow in simulation to the z axis. We found that $\Omega = (100.2 \pm 3.0)$ nm s^{-1} and $A = (5.5 \pm 1.2)$ nm s^{-1}. The ratio of the strength of the swirling flow to the toroidal one is $\Omega/A \approx 20$.

Simulation in oocyte-shaped geometry

To study the model in a geometry similar to the *Drosophila* oocyte, we construct a surface of revolution as

$$X = Dx$$
$$Y = Dr \cos(\phi) \tag{12}$$
$$Z = Dr \sin(\phi),$$

where $x \in (0, 1)$, $\phi \in [-\pi, \pi)$ and $r = \frac{Tx^{p_1}(1-x)^{p_2}}{2^{(1-p_1-p_2)}}$ (see ref. 49). l is the oocyte length, T sets the aspect ratio of the oocyte, and the parameters $p_1 \in [0, 1]$ and $p_2 \in [0, 1]$ determine the local curvature of the oocyte. In our simulations, we chose $D = 150$ μm, $T = 0.72$, $p_1 = 0.4$ and $p_2 = 0.2$.

Live imaging of the *Drosophila* oocyte

Young mated female adults were fed dry active yeast for 16–18 h and dissected in Halocarbon oil 700 (Sigma-Aldrich, catalogue no. H8898) as previously described[19,50]. Samples were imaged within 1 h after dissection using a Nikon W1 spinning disk confocal microscope (Yokogawa CSU with pinhole size 50 μm) with a Photometrics Prime 95B sCMOS Camera or Hamamatsu ORCA-Fusion Digital CMOS Camera and a ×40 1.25 numerical aperture silicone oil lens controlled by Nikon Elements software. 3D time lapses were acquired every 10 s at 1 μm per step. All oocytes were imaged with the AP axis parallel to the imaging plane.

Flies were maintained on standard cornmeal food (Nutri-Fly Bloomington Formulation, Genesee, catalogue no. 66-121) supplemented with dry active yeast (Red Star) at room temperature (24–25 °C). The following fly stocks were used in this study: mat αtub-Gal4[V37] (III, Bloomington *Drosophila* Stock Center, catalogue no. 7063)[51], UASp-F-Tractin-tdTomato (II, Bloomington Stock Center, catalogue no. 58989)[51,52], GFP::αtub (ref. 53).

Reconstruction of 3D velocity field from live imaging

Here, we describe the steps for 3D reconstruction of the velocity field and measurement of microtubule orientation from experimental images. First we reconstructed the 3D oocyte periphery, then we measured the 2D cytoplasmic velocity field for each z plane using particle image velocimetry, and then we used it to reconstruct the 3D velocity field. We also measured the local orientation of microtubules using a linear filter for texture analysis.

3D reconstruction of the oocyte periphery. We developed an active contour method[54,55] to partially reconstruct the 3D geometry of the oocyte from volumetric images of F-actin. We first segmented the oocyte periphery for each z plane and then used these to reconstruct the 3D oocyte surface. In short, for the middle z plane, we provided a closed curve, $\bar{\Gamma}(s)$, which serves as the initial guess for the active contour method. The shape of the oocyte in this z plane is given by minimizing the cost function

$$E[\Gamma(s)] = \oint_{\Gamma(s)} \frac{\alpha}{2} |\Gamma_{ss}|^2 \mathrm{d}s + \iint_R (I_N(x, y) - \beta) \mathrm{d}x \mathrm{d}y, \tag{13}$$

where $\Gamma_{ss} = \partial^2 \Gamma / \partial s^2$. The first term accounts for the smoothness of the contour, and the second term accounts for the interaction of the contour with the image, where β is set such that the contour expands if it is far from the periphery. The image intensity, $I_N(x, y)$, is the normalized smoothed gradient of the F-actin image. We then used the segmented shape of the oocyte in this z plane as an initial guess to segment the oocyte periphery in consecutive z planes.

2D particle image velocimetry. PIV is a common technique for inferring the local velocity of the fluid by measuring the displacement of tracer particles between two consecutive time points. In brightfield microscopy images of *Drosophila* oocytes, lipid granule particles have high contrast relative to the cytoplasm and can serve as tracer particles to measure local cytoplasmic velocity. We developed a platform to perform PIV on brightfield microscopy images of *Drosophila* oocytes. A key piece of our software is using the contrast-limited adaptive histogram equalization method to enhance the contrast of the brightfield images[56]. To accurately measure the velocity in the complex geometry of the oocyte, we combined fast Fourier transform-based PIV on a square grid within the interior of the oocyte and correlation-based PIV near the periphery.

For fast Fourier transform-based PIV, square boxes of 100 pixels with 20 pixel spacing were taken far from the oocyte periphery[57,58]. For each box, we calculated the Fourier transform of the image intensity for two consecutive time points, $\tilde{I}_t(u, v)$ and $\tilde{I}_{t+1}(u, v)$, calculated the Hadamard product of one with the complex conjugate of the other, $\tilde{I}_H = \tilde{I}_t \circ \tilde{I}_{t+1}^*$, and set the displacement in that box as the position of the maximum of the inverse Fourier transform of $I_H(\Delta x, \Delta y)$ (Supplementary Fig. 2a blue; pixel size, 0.260 μm).

For the correlation-based PIV for points near the periphery, we first constructed grids with shapes derived from the oocyte outline as follows: we chose N evenly spaced points on the periphery, and for each point, we constructed M evenly spaced points on a line connecting the centre of mass of the oocyte cross-section to that point. By connecting each set of points, we constructed $N \times M$ grids (Supplementary Fig. 2a). For each grid, we calculated the displacement by finding the maximum of the correlation function

$$H(\Delta_x, \Delta_y) = \int \int_A I_t(x, y) I_{t+1}(x + \Delta_x, y + \Delta_y) \mathrm{d}x \mathrm{d}y, \tag{14}$$

where I_t and I_{t+1} are the mean subtracted intensity and the integration is over the area of the grid. If there are several local maxima, we choose the one giving a smooth displacement field between the neighbouring grids. Finally, we use interpolation to estimate the planar components of the velocity field, $u_x(x, y, z)$ and $u_y(x, y, z)$, on a regular grid across the oocyte using these two displacement fields (Supplementary Fig. 2a).

Approximation of the out-of-plane velocity. We measured the out-of-plane component of the velocity field, $u_z(x, y, z)$, by assuming the incompressibility of the cytoplasm and the impermeability of the oocyte boundary (Γ) (on the timescales of microscopy) and solving

$$\nabla \cdot \mathbf{u} = 0; \quad \mathbf{u}|_\Gamma \cdot \mathbf{n} = 0, \tag{15}$$

where $\mathbf{n}$ is the unit surface normal vector. To do so, we numerically solve the ordinary differential equation

$$\frac{\partial u_z}{\partial z} = -\left(\frac{\partial u_x}{\partial x} + \frac{\partial u_y}{\partial y}\right), \tag{16}$$

with the boundary condition $u_z = -(n_x u_x + n_y u_y)/n_z$ at the oocyte periphery (Supplementary Fig. 2b, right).

Estimation of microtubule orientation field from microscopic images

To measure the local microtubule orientation, we use a Gabor filter, which is a linear filter for texture analysis[59]. It allows examination of any specific frequency content in the image in a given direction. The inputs of the filter are its wavelength and orientation, and the outputs are the magnitude and phase response to the filter. We use 3-pixel-wide wavelength for angles $\theta \in (0, \pi]$ with interval $\pi/180$, and for each angle, we calculate the magnitude response in grids of 20×20 pixels. We set the grid orientation as the angle with the largest magnitude response and the grid magnitude as the value of the magnitude response to that angle (Supplementary Fig. 4).

Estimation of defect positions in simulations

As illustrated in Fig. 2e, near the defect centres, microtubules are relatively straight and normal to the surface. To find the defect positions in the oocyte simulation, we sort all the microtubules in descending order of a_i (Supplementary Information equation (6)), the length of projection of the end–end vector on the surface. We assign the first defect centre to be at the location where the microtubule with lowest a_i is clamped. From the rest of the microtubules, we find the one with the next-lowest a_i that is at least 40 µm from the first defect and assign its clamping position to be the second defect.

Reporting summary

Further information on the research design is available in the Nature Portfolio Reporting Summary linked to this article.

Data availability

Simulational and experimental data sets generated during the current study are available from the corresponding author on reasonable request.

Code availability

A publicly available and elaborated version of the SkellySim codebase used to generate the simulations is available at https://github.com/flatironinstitute/SkellySim.

References

48. Greengard, L. & Rokhlin, V. A fast algorithm for particle simulations. *J. Comput. Phys.* **73**, 325–348 (1987).
49. Stoddard, M. C. et al. Avian egg shape: form, function, and evolution. *Science* **356**, 1249–1254 (2017).
50. Lu, W. et al. Ooplasmic flow cooperates with transport and anchorage in *Drosophila* oocyte posterior determination. *J. Cell Biol.* **217**, 3497–3511 (2018).
51. Lu, W., Lakonishok, M. & Gelfand, V. I. Gatekeeper function for short stop at the ring canals of the *Drosophila* ovary. *Curr. Biol.* **31**, 3207–3220.e4 (2021).
52. Spracklen, A. J., Fagan, T. N., Lovander, K. E. & Tootle, T. L. The pros and cons of common actin labeling tools for visualizing actin dynamics during *Drosophila* oogenesis. *Dev. Biol.* **393**, 209–226 (2014).
53. Grieder, N. C., De Cuevas, M. & Spradling, A. C. The fusome organizes the microtubule network during oocyte differentiation in *Drosophila*. *Development* **127**, 4253–4264 (2000).
54. Kass, M., Witkin, A. & Terzopoulos, D. Snakes: active contour models. *Int. J. Comput. Vis.* **1**, 321–331 (1988).
55. Farhadifar, R. & Needleman, D. in *Mitosis: Methods and Protocols* (ed. Sharp, D.) Ch. 3 (Springer, 2014).
56. Zuiderveld, K. in *Graphics Gems IV* (ed. Heckbert, P. S.) 474–485 (1994).
57. Willert, C. E. & Gharib, M. Digital particle image velocimetry. *Exp. Fluids* **10**, 181–193 (1991).
58. Thielicke, W. & Stamhuis, E. PIVlab—towards user-friendly, affordable and accurate digital particle image velocimetry in MATLAB. *J. Open Res. Softw.* **2**, e30 (2014).
59. Jain, A. K. & Farrokhnia, F. Unsupervised texture segmentation using gabor filters. *Pattern Recognit.* **24**, 1167–1186 (1991).

Acknowledgements

Author contributions

M.J.S., S.Y.S. and V.I.G. designed the research. S.D., R.F., G.K. and R.B. contributed to simulation software development and simulation data analysis. W.L. and M.L. designed and performed the experiments. S.D., R.F. and M.J.S. developed the image processing software and analysis of experimental data. S.D., R.F., S.Y.S. and M.J.S. prepared the manuscript. All authors contributed to its editing.

Competing interests

The authors declare no competing interests.

Additional information

Supplementary information The online version contains supplementary material available at https://doi.org/10.1038/s41567-023-02372-1.

Correspondence and requests for materials should be addressed to Michael J. Shelley.

Peer review information *Nature Physics* thanks Camille Duprat, Gerhard Gompper and the other, anonymous, reviewer(s) for their contribution to the peer review of this work.

Reprints and permissions information is available at www.nature.com/reprints.

nature portfolio

Corresponding author(s):   Michael J. Shelley

Last updated by author(s):   11/30/2023

Reporting Summary

Nature Portfolio wishes to improve the reproducibility of the work that we publish. This form provides structure for consistency and transparency in reporting. For further information on Nature Portfolio policies, see our Editorial Policies and the Editorial Policy Checklist.

Statistics

For all statistical analyses, confirm that the following items are present in the figure legend, table legend, main text, or Methods section.

n/a	Confirmed	
☐	☒	The exact sample size (n) for each experimental group/condition, given as a discrete number and unit of measurement
☐	☒	A statement on whether measurements were taken from distinct samples or whether the same sample was measured repeatedly
☒	☐	The statistical test(s) used AND whether they are one- or two-sided *Only common tests should be described solely by name; describe more complex techniques in the Methods section.*
☒	☐	A description of all covariates tested
☒	☐	A description of any assumptions or corrections, such as tests of normality and adjustment for multiple comparisons
☒	☐	A full description of the statistical parameters including central tendency (e.g. means) or other basic estimates (e.g. regression coefficient) AND variation (e.g. standard deviation) or associated estimates of uncertainty (e.g. confidence intervals)
☒	☐	For null hypothesis testing, the test statistic (e.g. F, t, r) with confidence intervals, effect sizes, degrees of freedom and P value noted *Give P values as exact values whenever suitable.*
☒	☐	For Bayesian analysis, information on the choice of priors and Markov chain Monte Carlo settings
☒	☐	For hierarchical and complex designs, identification of the appropriate level for tests and full reporting of outcomes
☒	☐	Estimates of effect sizes (e.g. Cohen's d, Pearson's r), indicating how they were calculated

Our web collection on statistics for biologists contains articles on many of the points above.

Software and code

Policy information about availability of computer code

Data collection	Simulations in this study were done using a specialized open-source codebase, SkellySim (developed at the Flatiron Institute), for simulating large assemblies of hydrodynamically coupled fibers. SkellySim is available at https://github.com/flatironinstitute/SkellySim.
Data analysis	Analysis of the simulation output was performed by using custom Matlab scripts, and SkellySim modules. Graphics was generated by custom Matlab and Blender scripts. Particle image velocimetry and analysis of microtubule orientation fields was performed using custom Matlab scripts.

For manuscripts utilizing custom algorithms or software that are central to the research but not yet described in published literature, software must be made available to editors and reviewers. We strongly encourage code deposition in a community repository (e.g. GitHub). See the Nature Portfolio guidelines for submitting code & software for further information.

Data

Policy information about availability of data

All manuscripts must include a data availability statement. This statement should provide the following information, where applicable:
- Accession codes, unique identifiers, or web links for publicly available datasets
- A description of any restrictions on data availability
- For clinical datasets or third party data, please ensure that the statement adheres to our policy

Simulational and experimental data sets generated during the current study are available from the corresponding author upon reasonable request.

Human research participants

Policy information about <u>studies involving human research participants and Sex and Gender in Research.</u>

Reporting on sex and gender	N/A
Population characteristics	N/A
Recruitment	N/A
Ethics oversight	N/A

Note that full information on the approval of the study protocol must also be provided in the manuscript.

Field-specific reporting

Please select the one below that is the best fit for your research. If you are not sure, read the appropriate sections before making your selection.

☒ Life sciences   ☐ Behavioural & social sciences   ☐ Ecological, evolutionary & environmental sciences

For a reference copy of the document with all sections, see <u>nature.com/documents/nr-reporting-summary-flat.pdf</u>

Life sciences study design

All studies must disclose on these points even when the disclosure is negative.

Sample size	Reported when applicable,
Data exclusions	No data was excluded.
Replication	N/A
Randomization	N/A
Blinding	N/A

Reporting for specific materials, systems and methods

We require information from authors about some types of materials, experimental systems and methods used in many studies. Here, indicate whether each material, system or method listed is relevant to your study. If you are not sure if a list item applies to your research, read the appropriate section before selecting a response.

Materials & experimental systems

n/a	Involved in the study
☒	☐ Antibodies
☒	☐ Eukaryotic cell lines
☒	☐ Palaeontology and archaeology
☐	☒ Animals and other organisms
☒	☐ Clinical data
☒	☐ Dual use research of concern

Methods

n/a	Involved in the study
☒	☐ ChIP-seq
☒	☐ Flow cytometry
☒	☐ MRI-based neuroimaging

Animals and other research organisms

Policy information about <u>studies involving animals</u>; <u>ARRIVE guidelines</u> recommended for reporting animal research, and <u>Sex and Gender in Research</u>

Laboratory animals	Fruit fly Drosophila melanogaster. The following fly stocks were used in this study: mat αtub-Gal4 [V37] (III, Bloomington Drosophila Stock Center #7063) ; UASp-F-Tractin-tdTomato (II, Bloomington stock center #58989) ; Jupiter-GFP (protein trap lineZCL2183, III) .
Wild animals	N/A

Reporting on sex	The oocytes are found in female organism only.
Field-collected samples	N/A
Ethics oversight	IACUC

Note that full information on the approval of the study protocol must also be provided in the manuscript.